

Research Article

Singular Perturbation Theory-Based Qualitative Dynamics Investigation of Flywheel Energy Storage System in Discharge Mode

Weiya Zhang,^{1,2} Yongli Li,^{1,2} Xiaoyong Chang,^{1,2} and Nan Wang^{1,2}

¹ Key Laboratory of Smart Grid of Ministry of Education, Tianjin University, Tianjin 300072, China

² School of Electrical Engineering and Automation, Tianjin University, Tianjin 300072, China

Correspondence should be addressed to Weiya Zhang; zhangweiyatju@126.com

Received 16 January 2014; Accepted 5 June 2014; Published 3 August 2014

Academic Editor: H. D. Chiang

Copyright © 2014 Weiya Zhang et al. This is an open access article distributed under the Creative Commons Attribution License, which permits unrestricted use, distribution, and reproduction in any medium, provided the original work is properly cited.

An investigation on qualitative dynamics in a voltage-current dual-loop controlled flywheel energy storage system (FESS) operating in discharge mode is presented in this paper, providing novel insights into the effect of two-timescale characteristics on the safety and stability of energy transmission of FESS. Based on singular perturbation theory, a two-timescale approach is proposed to separate the FESS into the fast and slow subsystems. Stability analysis of the transient fixed points confirms the effects of systemic parameters on FESS's dynamics and indicates that the FESS shifts from the spiking state to the quiescent state when the slow variable crosses the bifurcation point of the fast subsystem. Mechanism analysis reveals that the root cause of the qualitative dynamics is the voltage instability of the FESS. Moreover, the feasibility boundaries of key parameters are derived, and application requirements of the proposed approach are also discussed, guiding the extension of the approach to engineering applications and solving the dynamics analysis problem to some extent at a theoretical analysis level. Constant voltage discharge experiment is performed based on the FESS test bench built in Key Laboratory of Smart Grid of Ministry of Education, Tianjin University, which validates the theoretical results.

1. Introduction

Permanent magnet (PM) brushless dc motor (BLDCM) controlled FESS, with the advantages of high density, low maintenance, long lifetime, and good compactness, has become a new trend for energy storage, applied more and more in the uninterruptible power supply, rail transportation, and smart grids [1, 2]. As shown in Figure 1, the FESS mainly consists of two self-contained parts, that is, the mechanical part (flywheel motor system) and the electrical part (power drive system). In general, the flywheel motor is controlled by power electronic circuits. Due to the existence of the intrinsic nonlinearity, various nonlinear dynamics occur during the operation of FESS when the system state changes, which has an influence on the safety and stability of energy transmission.

So far, rotor dynamic problems of FESS's mechanical part have been seen as a cause of decreased rotor dynamic performance and reduced stability [3–9]. However, few researchers have revealed that, as a strongly coupled system, FESS has

more complex nonlinear dynamics due to the interaction and difference between the mechanical part and the electrical part. This complex nonlinear dynamics has much more direct influence on the safety and stability of energy transmission and thus affects the safety and stability of FESS. Zhang et al. have investigated the nonlinear dynamics of FESS from the viewpoint of the interaction between the mechanical part and the electrical part [10]. Turning to the difference of the two parts we find that the electrical variables have significantly faster dynamics than the mechanical variables. As such, the dynamics of the voltage and current are faster than that of the rotate speed of flywheel, making the FESS be a typical two-timescale system [11]. It is well known that bursting phenomenon is observed when a slow variable controls the fast dynamics in some two-timescale systems such as neuronal systems and biological systems [12, 13]. Bursting is a state of switching between the spiking state (SP) and the quiescent state (QS). Generally, QS indicates all the variables are at rest or exhibit small amplitude oscillations,

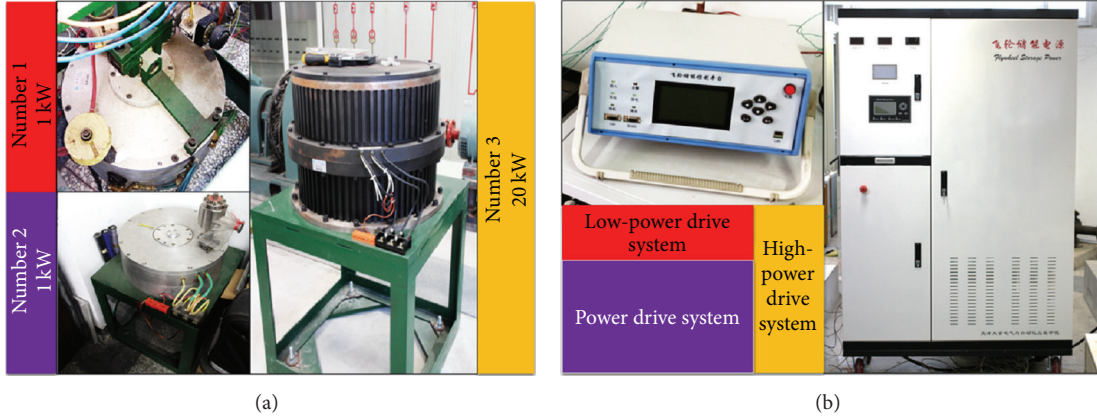


FIGURE 1: FESS test bench. (a) Flywheel motor system, (b) power drive system.

while SP indicates variables may behave in large amplitude oscillations.

In this paper, we aim to present evidences that as FESS operating in discharge mode, a small change in parameter values around the bifurcation points of FESS's fast system will lead to qualitative dynamics of the full-system, and investigate the effect of two-timescale characteristics on such dynamics, which is similar to nonrecurrent bursting. The analysis of dynamical systems with two timescales is a subject whose history interweaves three different viewpoints: non-standard analysis [14], classical asymptotics [15], and geometric singular perturbation theory [16]. The first two methods lead to relatively large errors, and the geometric singular perturbation method is used to get the analytical solution of simple multiple timescale systems. The two-timescale approach proposed by Rinzel [17] is the classic approach to deeply investigate the two-timescale bifurcation dynamics, which gives a full description of the steady state, and periodic solution set of the fast subsystem, reflecting the global bifurcation structure of the fast subsystem with the slow variables treated as parameters [18]. First, stability analysis of the transient fixed points is proposed to study the bifurcation set of the fast subsystem, showing that as the slow variable varies, the fast subsystem loses stability from the originally stable state to Hopf bifurcation, and the dynamical evolution of the full-system is close in accordance with that of the fast subsystem. Not only revealing that the operation state of the FESS shifts when the slow variable crosses the bifurcation point of the fast subsystem, but also giving a way to predict the occurrence and evolution of qualitative dynamics of FESS in discharge mode. Then, the bifurcation mechanism analysis of the fast subsystem is proposed, offering an intuitive explanation of the origin of the nonrecurrent dynamics of the full-system. Furthermore, the feasibility regions are shown and provide instructions to parameters setting of FESS. Finally, the application requirements of the proposed approach are also discussed, guiding the extension of the approach to dynamics analysis of other electromechanical coupling systems.

This paper is organized as follows. In Section 2, the normalized dynamic model of FESS is established and numerical simulations have been taken. In Section 3, the two-timescale approach based on singular perturbation theory is proposed

and applied. A brief analysis of the application of the proposed approach is shown in Section 4. Also, the observed instability phenomena are observed experimentally, as presented in Section 5. Finally, Section 6 concludes this paper.

2. Modelling and Two-Timescale Characteristics of FESS

As shown in Figure 2, the modelling of FESS includes the flywheel motor system (the flywheel rotor driven by BLDCM) and the power drive system (the electrical subsystem and feedback control subsystem). The flywheel motor system is designed with a full bridge (IGBTs) at its output electrical terminals and DC-DC converter at the dc link. While diodes perform uncontrolled rectification, the DC-DC converter adjusts the voltage of the BLDCM in order to make it suitable for the load. Electronic commutation is achieved using a microprocessor-based controller with a Hall-effect position and a current sensor as input to generate gating signals for IGBTs.

2.1. Modelling of FESS. Before modeling the FESS, five assumptions of the flywheel motor system are described as follows: (a) the saturation of the core is neglected; (b) the losses of eddy and hysteresis are ignored; (c) the distribution of air gap is uniform; (d) the self-inductance and mutual inductance among the windings are independent of the position of the rotor; (e) ignore the commutation process. The physical structure of the flywheel motor system is shown in Figure 3(a), while the schematic diagram is shown in Figure 3(b). It has been assumed that the phase resistance r_m , the self-inductance L , and mutual inductance M of all the windings are equal. Assuming further that there is no change in the rotor reluctance with angle, hence, the circuit equations of the three windings in phase variables are

$$\begin{bmatrix} e_a \\ e_b \\ e_c \end{bmatrix} = \begin{bmatrix} r_m & 0 & 0 \\ 0 & r_m & 0 \\ 0 & 0 & r_m \end{bmatrix} \begin{bmatrix} i_A \\ i_B \\ i_C \end{bmatrix} + \begin{bmatrix} L & M & M \\ M & L & M \\ M & M & L \end{bmatrix} \frac{d}{dt} \begin{bmatrix} i_A \\ i_B \\ i_C \end{bmatrix} + \begin{bmatrix} u_A \\ u_B \\ u_C \end{bmatrix}, \quad (1)$$

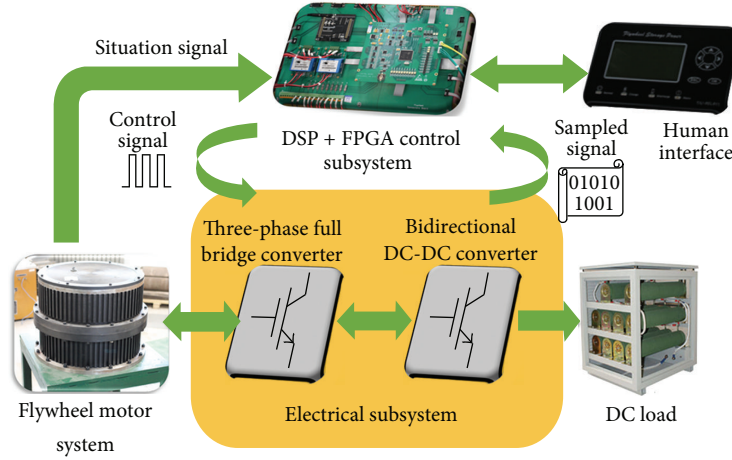


FIGURE 2: Structure of the FESS.

where u_A , u_B , and u_C are phase voltages, i_A , i_B , and i_C are phase currents, and e_a , e_b , and e_c are the induced back EMFs. For $i_A + i_B + i_C = 0$ and denoting $L - M$ as l_m , then the coupled circuit of the stator windings in terms of the machine electrical constants can be derived in Figure 3(c). The circuit equation can be written as

$$\begin{bmatrix} e_a \\ e_b \\ e_c \end{bmatrix} = \begin{bmatrix} r_m & 0 & 0 \\ 0 & r_m & 0 \\ 0 & 0 & r_m \end{bmatrix} \begin{bmatrix} i_A \\ i_B \\ i_C \end{bmatrix} + \begin{bmatrix} l_m & 0 & 0 \\ 0 & l_m & 0 \\ 0 & 0 & l_m \end{bmatrix} \frac{d}{dt} \begin{bmatrix} i_A \\ i_B \\ i_C \end{bmatrix} + \begin{bmatrix} u_A \\ u_B \\ u_C \end{bmatrix}. \quad (2)$$

According to the switching pattern (commutation function), only two phases are active at the same time, while the third one is silent (Figure 3(d)) [19]. For example, the voltage equation during the operation of phase A-B can be written as

$$\begin{aligned} u_2 &= -2r_m i_a - 2l_m \frac{di_a}{dt} + (e_A - e_B) \\ &= -R_m i_a - L_m \frac{di_a}{dt} + K_e \omega, \end{aligned} \quad (3)$$

where K_e , B_v , J , $R_m = 2r_m$, and $L_m = 2l_m$ denote line back-EMF constant, friction coefficient, moment of inertia, line resistance, and line inductance, respectively. Considering the equation of motion for BLDCM and treating the susceptibility and flux as constant, the differential equations for flywheel motor system are derived as

$$\begin{aligned} \frac{di_a}{dt} &= \frac{K_e \omega}{L_m} - \frac{R_m i_a}{L_m} - \frac{u_2}{L_m}, \\ \frac{d\omega}{dt} &= -\frac{K_m i_a}{J} - \frac{B_v \omega}{J}, \end{aligned} \quad (4)$$

where K_m denotes torque constant and the angular velocity ω , the phase current i_a , and the motor voltage u_2 are state variables.

TABLE 1: Nomenclature for state variables.

State variables (with dimensions)	State variables (dimensionless)
Inductor current i_L	$X_1(i_L)$
Load voltage u_1	$X_2(u_1)$
Motor voltage u_2	$X_3(u_2)$
Phase current i_a	$X_4(i_a)$
Angular velocity ω	$X_5(\omega)$
Outer corrector output x_{1c}	$X_6(x_{1c})$
Inner corrector output x_{2c}	$X_7(x_{2c})$

TABLE 2: Nomenclature for abbreviations.

Systematic matrix coefficient	Input matrix coefficient
$a_1, a_2, a_3, a_4, a_5, a_6, a_7, a_8, a_9, a_{10}, a_{11}$	b_1, b_2

As shown in Figure 4, the electrical subsystem include a bidirectional DC-DC converter, which consists of a transfer inductor L , capacitors C_1 and C_2 , IGBT V_1 with diode VD_1 , and IGBT V_2 with diode VD_2 and a three-phase full bridge converter which consists of IGBT-diode VT_{1-6} . Mechanical energy is converted into electrical energy through the diodes of the three-phase full bridge converter when electrical energy is transmitted to the load via bidirectional DC-DC converter and regulated as load demands. During the discharge mode, the switching of V and VD determines the two different modes, which are Mode 1 ($nT < t < nT + dT$) when V_2 is on and VD_1 is off and Mode 2 ($nT + dT < t < (n+1)T$) when V_2 is off and VD_1 is on. A dual-loop proportional-integral scheme is applied to regulate the duty cycle of switches, of which the PI coefficients are (K_{pv}, K_{iv}) and (K_{pi}, K_{ii}) . The sampling coefficients of voltage and current are $h_v = 0.02424$ and $h_i = 0.08$.

Dimensionless parameters are introduced to put the system into standard form. Define the nominal output voltage as V_{ref} , the nominal angular velocity as ω_{ref} , and the load resistance as R . To be clear, the nomenclature for all variables, abbreviations, and parameters are listed in Tables 1, 2, and 3. With these definitions, the other variables can be

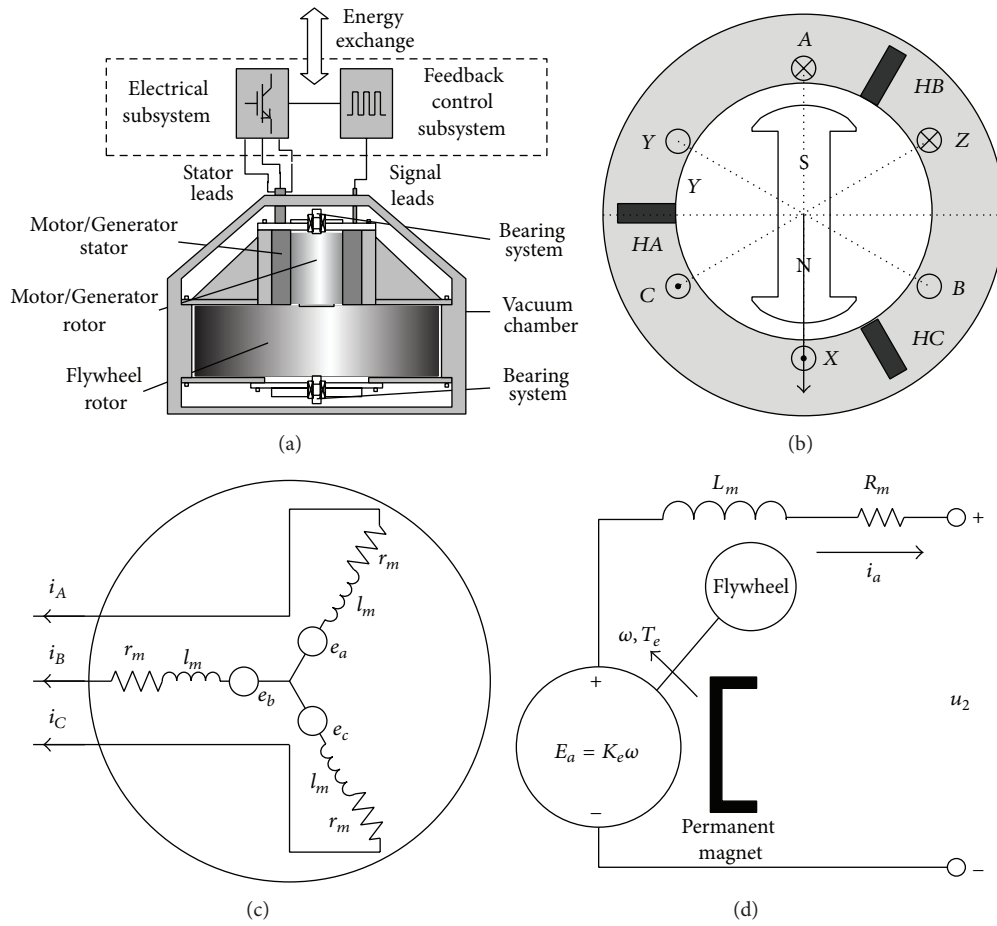


FIGURE 3: Flywheel motor system: (a) physical structure, (b) schematic diagram, (c) three-phase equivalent circuit, (d) two-phase conducting equivalent circuit (the current direction corresponds to the generator operation).

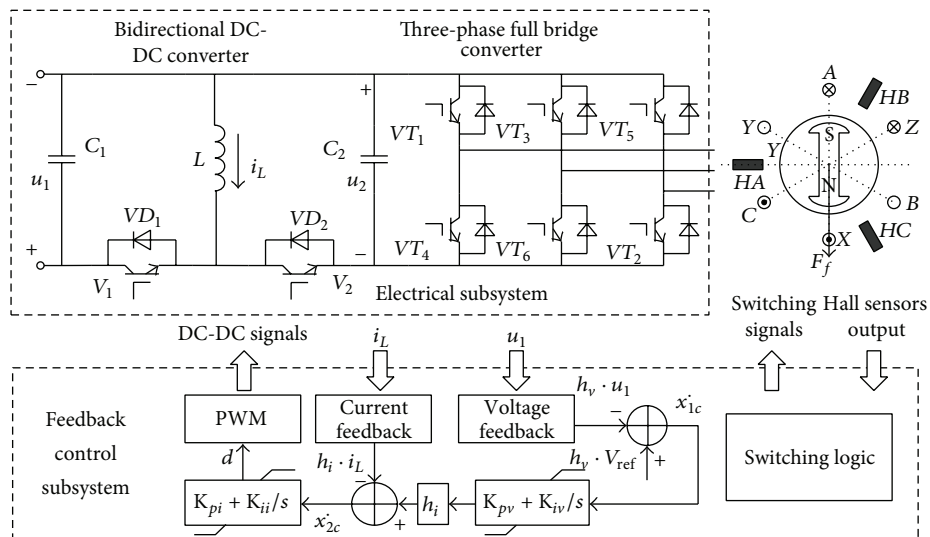


FIGURE 4: Schematic diagram of power drive system.

TABLE 3: Nomenclature for parameters with values.

Parameter	Value
Voltage-loop K_{pv}	60
Voltage-loop K_{iv}	49
Current-loop K_{pi}	40
Current-loop K_{ii}	36
Nominal angular velocity ω_{ref}	800 rads^{-1}
Transfer inductance L	0.7 mH
Filter capacitance C_1	1 mF
Filter capacitance C_2	1 mF
Line resistance R_m	0.5 Ω
Line inductance L_m	0.36 mH
Torque constant K_m	0.0673 Nm/A
Line back-EMF constant K_e	0.0625 V/rads $^{-1}$
Friction coefficient B_v	0.0001 Nm/rads $^{-1}$
Moment of inertia J	0.123 kgm^2
Load resistance R	5 Ω

normalized on the basis of $t = \sqrt{LC_1}\tau$, $X_1(i_L) = i_L R/V_{ref}$, $X_2(u_1) = u_1/V_{ref}$, $X_3(u_2) = u_2/V_{ref}$, $X_4(i_a) = i_a R/V_{ref}$, $X_5(\omega) = \omega/\omega_{ref}$, $X_6(x_{1c}) = x_{1c}$, $X_7(x_{2c}) = x_{2c}$, $a_1 = R\sqrt{LC_1}/L$, $a_2 = -\sqrt{LC_1}/(RC_1)$, $a_3 = \sqrt{LC_1}/(RC_2)$, $a_4 = RK_e\omega_{ref}\sqrt{LC_1}/(V_{ref}L_m)$, $a_5 = -R_m\sqrt{LC_1}/L_m$, $a_6 = -R\sqrt{LC_1}/L_m$, $a_7 = -K_m V_{ref}\sqrt{LC_1}/(JR\omega_{ref})$, $a_8 = -B_v\sqrt{LC_1}/J$, $a_9 = h_v V_{ref}\sqrt{LC_1}$, $a_{10} = -h_i V_{ref}\sqrt{LC_1}/R$, $a_{11} = -K_{pv}h_v h_i V_{ref}\sqrt{LC_1}$, $a_{12} = K_{iv}h_i\sqrt{LC_1}$, $b_1 = a_9$, and $b_2 = -a_{11}$.

Then, the dimensionless switched dynamical equations of the present FESS are

$$\begin{aligned} \dot{\mathbf{X}}(\tau) &= \mathbf{A}_1 \mathbf{X}(\tau) + \mathbf{B}_1, \quad \text{Mode 1,} \\ \dot{\mathbf{X}}(\tau) &= \mathbf{A}_2 \mathbf{X}(\tau) + \mathbf{B}_2, \quad \text{Mode 2,} \end{aligned} \quad (5)$$

where

$$\mathbf{A}_1 = \begin{bmatrix} 0 & 0 & a_1 & 0 & 0 & 0 & 0 \\ 0 & a_2 & 0 & 0 & 0 & 0 & 0 \\ -a_3 & 0 & 0 & a_3 & 0 & 0 & 0 \\ 0 & 0 & a_6 & a_5 & a_4 & 0 & 0 \\ 0 & 0 & 0 & a_7 & a_8 & 0 & 0 \\ 0 & -a_9 & 0 & 0 & 0 & 0 & 0 \\ a_{10} & a_{11} & 0 & 0 & 0 & a_{12} & 0 \end{bmatrix},$$

$$\mathbf{A}_2 = \begin{bmatrix} 0 & -a_1 & 0 & 0 & 0 & 0 & 0 \\ -a_2 & a_2 & 0 & 0 & 0 & 0 & 0 \\ 0 & 0 & 0 & a_3 & 0 & 0 & 0 \\ 0 & 0 & a_6 & a_5 & a_4 & 0 & 0 \\ 0 & 0 & 0 & a_7 & a_8 & 0 & 0 \\ 0 & -a_9 & 0 & 0 & 0 & 0 & 0 \\ a_{10} & a_{11} & 0 & 0 & 0 & a_{12} & 0 \end{bmatrix},$$

$$\mathbf{B}_1 = \mathbf{B}_2 = \begin{bmatrix} 0 \\ 0 \\ 0 \\ 0 \\ 0 \\ b_1 \\ b_2 \end{bmatrix},$$

$\mathbf{X}(\tau)$

$$= [X_1(i_L) \ X_2(u_1) \ X_3(u_2) \ X_4(i_a) \ X_5(\omega) \ X_6(x_{1c}) \ X_7(x_{2c})]^T. \quad (6)$$

2.2. Dynamic Characteristics. The operation principle of FESS is concerned with two processes: charge and discharge. In the charge mode, the flywheel motor system is driven by power grid and the electric energy is stored in the form of mechanical energy. Once the unit receives a signal of discharge, the flywheel rotor starts to decelerate and drives the BLDCM to generate electricity. This paper reports that the parametric regions have a significant effect on the two-timescale characteristics of FESS and the discharge performance degrades due to nonlinear dynamics when FESS's systemic parameters fall into a certain area.

Here, based on the exact state (5), a series of numerical simulations are carried out to make an initial evaluation of the possible dynamics. As shown in Table 3, the physical system parameters are set according to the actual FESS, and the PI control parameters of the feedback control subsystem are carefully designed to maintain closed-loop performance of the power drive system in spite of varying conditions. For energy storage unit as FESS, the stability in conjunction with the discharge targets is the primary consideration, so we restrict our attention to the case when V_{ref} varies, while the other parameters are fixed. Essentially, for each set of parameters, cycle-by-cycle time domain waveforms are generated by solving the appropriate linear equation in a subinterval of time, according to different switching states. The waveforms for different V_{ref} are shown in Figures 5–7.

Figure 5(a) shows that at $V_{ref} = 5\text{ V}$, $X_1(i_L)$ takes a combined oscillation of large and small amplitudes as the flywheel rotor slows down. At the beginning of discharge, $X_1(i_L)$ shows a quasiperiodic oscillation with a high-value magnitude. Such oscillations decay rapidly when $X_5(\omega)$ drops to 0.5; then $X_1(i_L)$ becomes steady. The close-up views are shown in Figures 5(b)–5(c). Dynamics of $X_3(u_2)$ and $X_2(u_1)$ as $X_5(\omega)$ decreases are shown in Figure 5(d). For $V_{ref} = 10\text{ V}$ and $V_{ref} = 15\text{ V}$ shown in Figures 6–7, similar oscillations with different amplitudes and frequencies happen to $X_1(i_L)$. Although the control parameters are carefully designed according to the closed-loop transfer function of the power drive system, the interaction and difference between the mechanical part and the electrical part still cause complex nonlinear dynamics. It can be seen that larger V_{ref} determines stronger oscillations and $X_5(\omega)$ changes much slower than other state variables. This indicates the existence of two-timescale characteristics in the discharge mode of FESS. Moreover, the oscillations of the electrical variables weaken

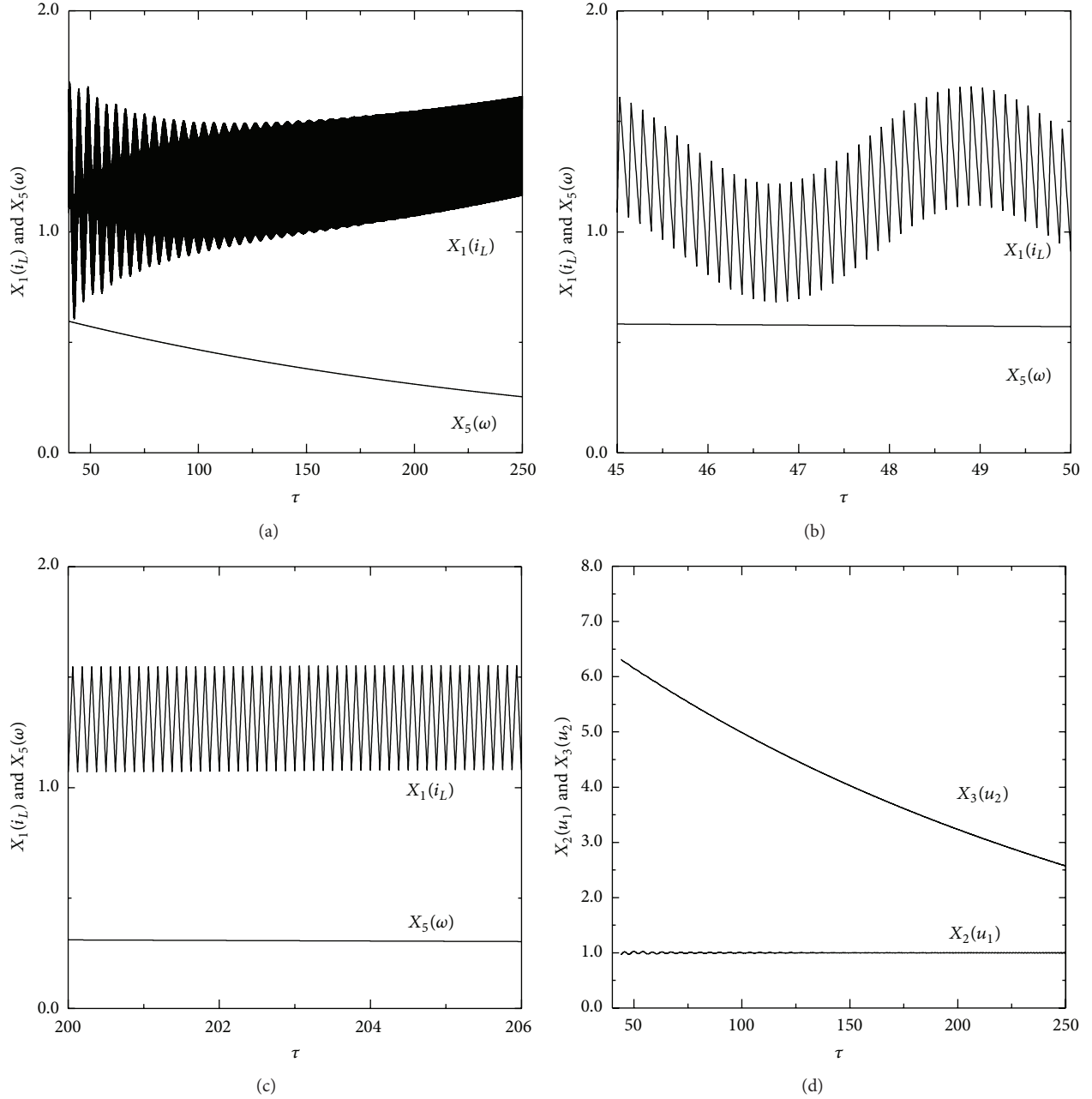


FIGURE 5: Time histories at $V_{\text{ref}} = 5$ V, for (a) $X_1(i_L)$, (b) oscillatory state of (a), (c) steady state of (a), (d) $X_2(u_1)$ & $X_3(u_2)$.

along with the decrease of the mechanical variables, which will be proved related to the qualitative dynamics in the following section.

3. Singular Perturbation Theory-Based Qualitative Dynamics Analysis

In this section, based on the singular perturbation theory, the two-timescale approach is proposed to separate the full-system into the fast and slow subsystems, providing a way for analyzing the interaction of the two-timescale dynamics. Treating the slow variable as constant, stability analysis of

the transient fixed points of the full-system is proposed to describe the evolution of dynamics of the full process.

3.1. Two-Timescale Model. Averaged model approach is a common method to analyze the physical mechanism of converters which neglects the switching details but focuses on the envelope of the dynamical motion. The following analysis will adopt this approach. Set the duty ratio as d . Set all the derivatives to zero, and we get

$$\dot{X}_1(i_L) = (d-1)a_1X_2(U_1) + da_1X_3(U_2) = 0,$$

$$\dot{X}_2(U_1) = (d-1)a_2X_1(i_L) + a_2X_2(U_1) = 0,$$

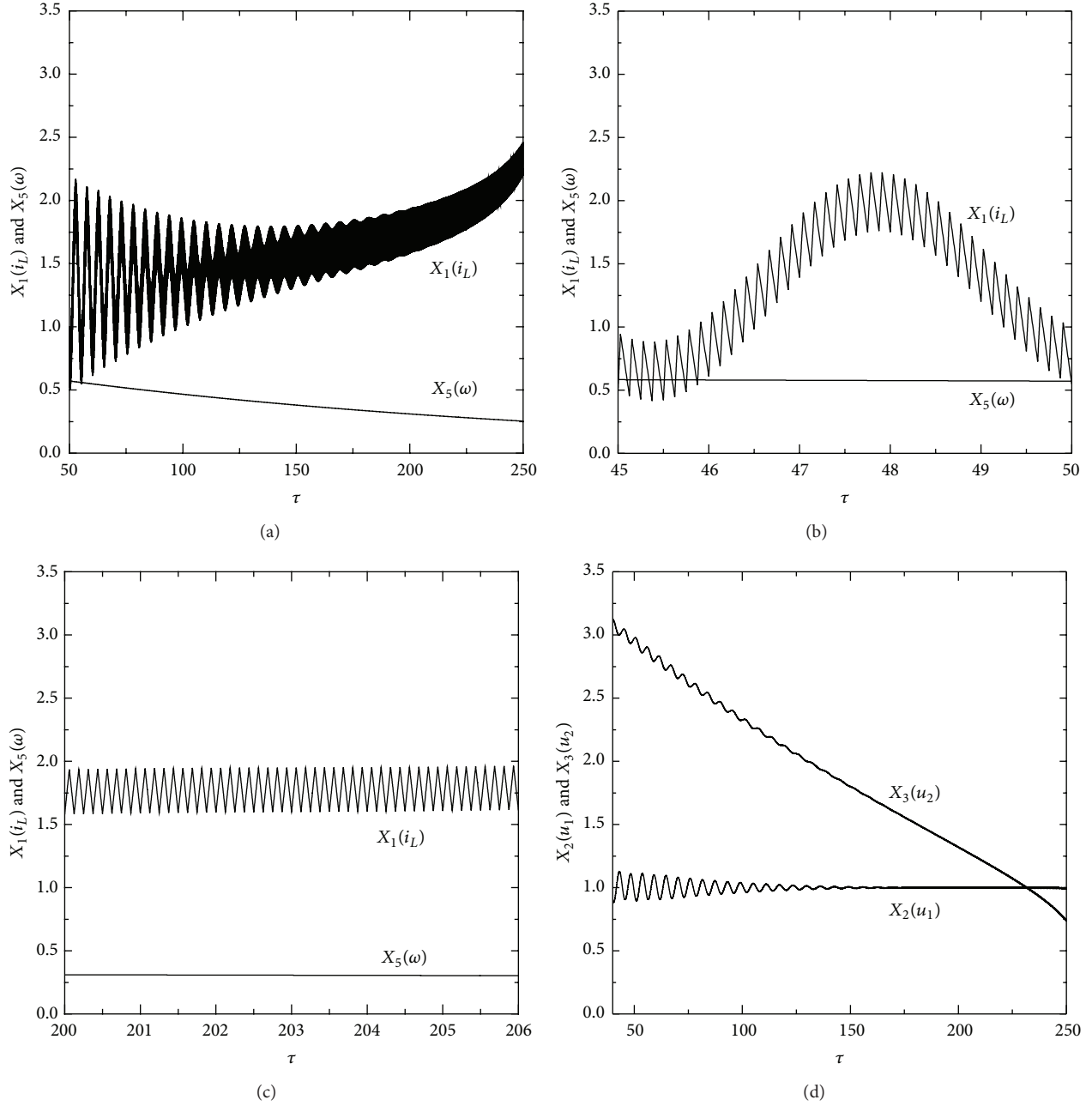


FIGURE 6: Time histories at $V_{\text{ref}} = 10$ V, for (a) $X_1(i_L)$, (b) oscillatory state of (a), (c) steady state of (a), (d) $X_2(u_1)$ & $X_3(u_2)$.

$$\begin{aligned}
 \dot{X}_3(U_2) &= a_3 X_4(I_a) - d a_3 X_1(I_L) = 0, \\
 \dot{X}_4(I_a) &= a_4 X_5(\Omega) + a_5 X_4(I_a) + a_6 X_3(U_2) = 0, \\
 \dot{X}_5(\Omega) &= a_7 X_4(I_a) + a_8 X_5(\Omega) = 0, \\
 \dot{X}_6(X_{1c}) &= -a_9 X_2(U_1) + a_9 = 0, \\
 \dot{X}_7(X_{2c}) &= a_{10} X_1(I_L) + a_{11} X_2(U_1) + a_{12} X_6(X_{1c}) - a_{11} \\
 &= 0,
 \end{aligned}
 \tag{7}$$

where $X_1(I_L)$, $X_2(U_1)$, $X_3(U_2)$, $X_4(I_a)$, $X_5(\Omega)$, $X_6(X_{1c})$, and $X_7(X_{2c})$ are average values of $X_1(i_L)$, $X_2(u_1)$, $X_3(u_2)$, $X_4(i_a)$, $X_5(\omega)$, $X_6(x_{1c})$, and $X_7(x_{2c})$ during a duty cycle, U_{ramp} is the independent sawtooth peak voltage of the control subsystem, $a_{13} = K_{ii}/U_{\text{ramp}}$, $a_{14} = K_{pi}K_{pv}h_i/U_{\text{ramp}}$, $a_{15} = -K_{pi}K_{pv}h_vh_iV_{\text{ref}}/U_{\text{ramp}}$, $a_{16} = -K_{pi}h_vh_iV_{\text{ref}}/(RU_{\text{ramp}})$, and $d = a_{13}X_7(X_{2c}) + a_{14}X_6(X_{1c}) + a_{15}X_2(U_1) + a_{16}X_1(I_L) - a_{15}$. a_i ($i = 1, 2, \dots, 12$) are real constants with different magnitudes, among which a_7 and a_8 are about 100 times smaller than the others. Thus $X_5(\omega)$ changes much slower than other variables, which

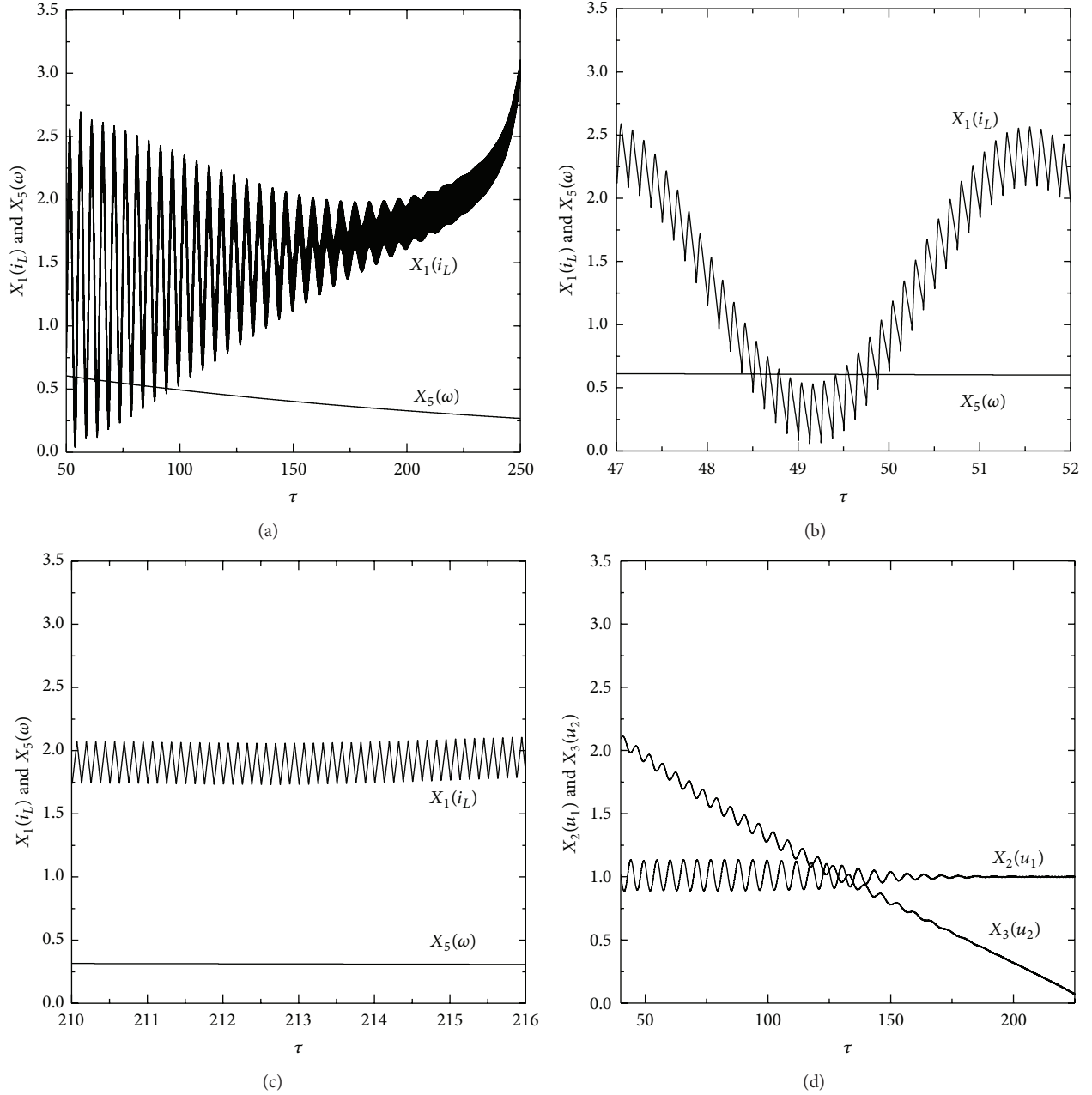


FIGURE 7: Time histories at $V_{\text{ref}} = 15 \text{ V}$, for (a) $X_1(i_L)$, (b) oscillatory state of (a), (c) steady state of (a), (d) $X_2(u_1)$ & $X_3(u_2)$.

proves the existence of state variables with two timescales. The full-system can be divided into fast subsystem and slow subsystem, that is, the fast subsystem α which contains $(X_1(i_L), X_2(u_1), X_3(u_2), X_4(i_a), X_6(x_{1c}), X_7(x_{2c}))$ and the slow subsystem β which contains $X_5(\omega)$. From (7) we can see a_4 reflects the coupling effect between $X_5(\omega)$ and $X_4(i_a)$ and also the coupling effect between the fast and slow subsystems. Define a_4 as coupling coefficient; the influence on dynamics of FESS from a_4 will be studied later.

3.2. Hopf Bifurcation Set for Fast Subsystem. To study the mechanism of the full-system's dynamics, the concept of transient fixed point is proposed; for general multitimescale system, define the transient fixed point of the full-system as the fixed point of the fast subsystem under slow variables with different fixed values. During a sufficiently short time period $[\tau_k, \tau_k + \Delta\tau]$, the movement trend of the fast subsystem during $[\tau_k, \tau_k + \Delta\tau]$ can be predicted by the eigenvalues on the basis at $\bar{X}_5 = X_5(\omega)|_{\tau_k}$. Thus the microstructure of the full trajectory can be described. The transient fixed point at various \bar{X}_5 is

$$[X_1 \ X_2 \ X_3 \ X_4 \ X_6 \ X_7]^T = \left[\frac{1}{1-D} \ 1 \ 1-D \ \frac{D}{1-D} \ \frac{a_{10}}{(D-1)a_{12}} \ \frac{1}{a_{13}} \left(D + \frac{a_{16}}{D-1} + \frac{a_{10}a_{14}}{(1-D)a_{12}} \right) \right]^T, \quad (8)$$

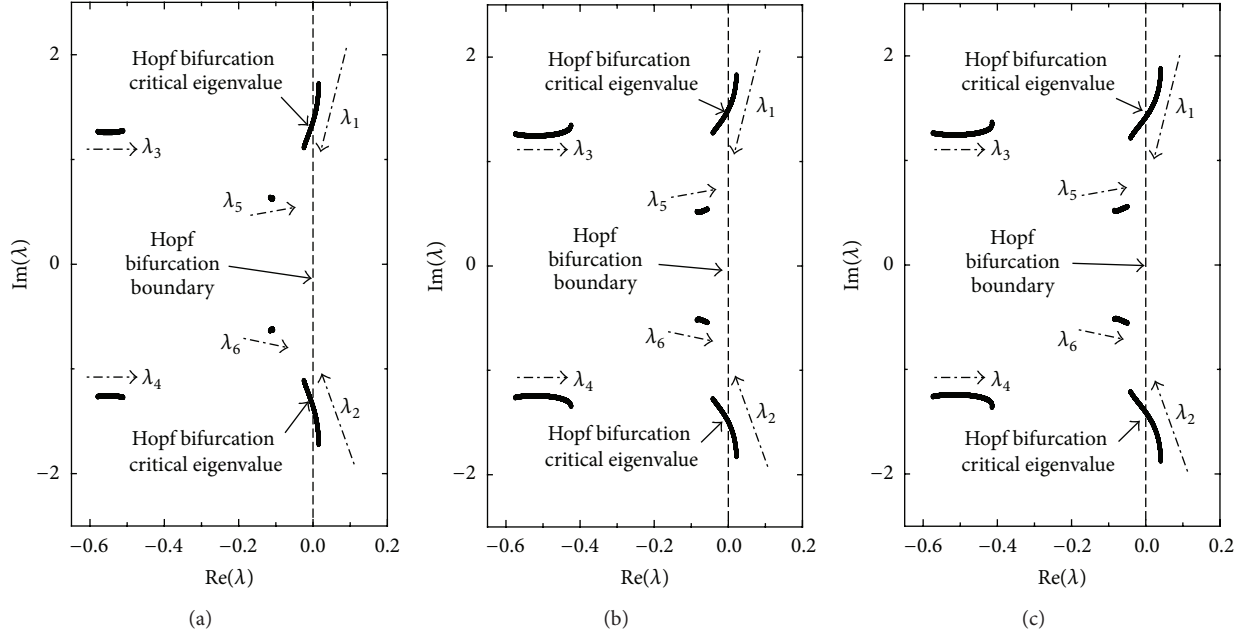


FIGURE 8: Eigenvalue loci as $\overline{X_5}$ decreases from 0.9 to 0.1 at (a) $V_{\text{ref}} = 5$ V, (b) $V_{\text{ref}} = 10$ V, and (c) $V_{\text{ref}} = 15$ V.

where $D = \frac{(2a_6 + a_4\overline{X_5} - a_5 + \sqrt{(a_5 - a_4\overline{X_5} - 2a_6)^2 - 4a_6(a_4\overline{X_5} + a_6)})}{2a_6}$.

By studying the movement of the eigenvalues of the Jacobian under varying $\overline{X_5}$, stability information such as the

occurrence of bifurcations can be obtained, which reveals the bifurcation of the transient fixed points follows:

$$\det[\lambda \mathbf{I} - \mathbf{J}(X)] = 0,$$

$$\mathbf{J}(X) = \begin{bmatrix} a_1 a_{16} (X_2 + X_3) & Da_1 - a_1 + a_1 a_{15} X_2 + a_1 a_{16} X_3 & Da_1 & 0 & a_1 a_{14} (X_2 + X_3) & a_1 a_{13} (X_2 + X_3) \\ Da_2 - a_2 + a_2 a_{16} X_1 & a_2 + a_2 a_{15} X_1 & 0 & 0 & a_2 a_{14} X_1 & a_2 a_{13} X_1 \\ -Da_3 - a_3 a_{16} X_1 & -a_3 a_{15} X_1 & 0 & a_3 & -a_3 a_{14} X_1 & -a_3 a_{13} X_1 \\ 0 & 0 & a_6 & a_5 & 0 & 0 \\ 0 & -a_9 & 0 & 0 & 0 & 0 \\ a_{10} & a_{11} & 0 & 0 & a_{12} & 0 \end{bmatrix}, \quad (9)$$

where λ is the eigenvalue, \mathbf{I} is the identity matrix, and $\mathbf{J}(X)$ is the Jacobian matrix at $[X_1, X_2, X_3, X_4, X_6, X_7]$. Parameters are set as Table 3, and loci of the eigenvalues are shown in Figure 8. When all the eigenvalues are in the left half-side of complex plane, the system is stable. When a couple of complex conjugate eigenvalues simultaneously cross the imaginary axis, Hopf bifurcation occurs [20, 21].

From Figures 8(a)–8(c), as $\overline{X_5}$ changes from 0.9 to 0.1, the eigenvalues ($\lambda_3, \lambda_4, \lambda_5, \lambda_6$) stay on the left half-side of complex plane, while a pair of conjugate complex eigenvalues (λ_1, λ_2) are firstly on the right half-side and cross the imaginary axis as $\overline{X_5}$ reaches 0.4903, 0.4269, and 0.3774, respectively.

3.3. Studies on Qualitative Dynamics. It would be imperative to know how the influence on the stability of the transient

fixed points from the slow variable is reflected in the full-system. The study of the internal relations between the properties of the transient fixed points and the full-system's dynamics can predict the occurrence and evolution of non-linear dynamics of FESS in the discharge mode. Among all the fast variables, the inductor current i_L serves as a link between the access system and the flywheel motor system; thus, the stability and dynamic characteristics of i_L influence the energy transmission process a lot. In this part we focus mainly on the dynamics of $X_1(i_L)$ against $X_5(\omega)$. Parameters are set as Table 3, and obviously in Figure 9, the transient fixed points curves (ES_1, ES_2 , and ES_3) are L-form curves with various $X_5(\omega)$, which is divided in a stable part (dashed line) and an unstable part (solid line). Hopf bifurcation points (H_1, H_2 , and H_3) are the joints of the two parts.

Considering the different kinds of equilibria, the stable node represents the quiescent state (QS), which indicates

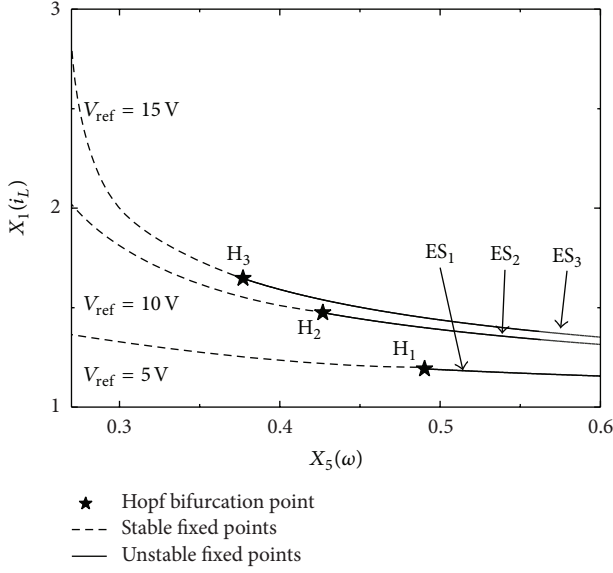


FIGURE 9: Transient fixed points curves (ES_1 , ES_2 , and ES_3) with the variation of $X_5(\omega)$ at $V_{ref} = 5$ V, 10 V, 15 V.

all the variables are at rest or exhibit small amplitude oscillations. The stable limit cycle surrounding the unstable focus represents the spiking state (SP), which indicates variables may behave in large amplitude oscillations [22]. Figures 10(a)–10(f) show the stroboscopic phase trajectory [23] of the full-system as well as the transient fixed points curves under different reference voltages in two and three dimensions. The phase trajectory for $V_{ref} = 5$ V is plotted in Figures 10(a)–10(b), from which we can see that H_1 divides the full-system's trajectory into two qualitatively different parts. Hopf bifurcation occurs at H_1 . The trajectory starting at A_1 moves along ES_1 to H_1 , where the trajectory tends to a limit cycle oscillation, the direction of which can be demonstrated by $\dot{X}_5(\omega)$ (see the expression in (7)). Between H_1 and A_1 , the difference between the fast and slow subsystems on timescales causes large amplitude oscillations around ES_1 from the beginning of the discharge process, leading the system to SP (from A_1 to H_1). The repetitive oscillation stays until the trajectory meets H_1 , at which Hopf bifurcation of the transient fixed point takes place. Using the center manifold theory, the curvature coefficient at the Hopf bifurcation point is less than 0, which proved the existence of supercritical bifurcation. Therefore, the amplitudes of the oscillations decrease gradually after the trajectory passing by H_1 and SP settles down to QS (from H_1 to B_1). The coupling strength of the fast and slow subsystems causes another type of small amplitude oscillations around ES_1 in QS. Then the phase trajectory reaches B_1 , at which the full-system becomes stable. When the FESS is in QS, the slow subsystem only influences the position of the transient fixed points but does not affect the dynamics of the full-system. For the reason that H_1 is the unique Hopf bifurcation point to join SP and QS, there is only one state conversion in a discharge cycle. The above process completes one period of the nonrecurrent qualitative dynamics.

Similar phenomena occur when the reference voltages are 10 V and 15 V. For $V_{ref} = 10$ V and 15 V in Figures 10(c)–10(f), the H_2 and H_3 still join SP and QS. Comparing with qualitative dynamics at $V_{ref} = 5$ V, the real part of the pair of complex conjugate eigenvalues of the Jacobian at the transient fixed point corresponding to A_2 and A_3 are larger than that corresponding to A_1 , which causes much more intense oscillations in SP. Above all, the slow variable modulates the qualitative dynamics by acting essentially as parameters to the full-system. The FESS shifts from SP to QS with the change of the slow variable. These shifts occur when the slow variable crosses the bifurcation point on the transient fixed points curve. Furthermore, from the expression of a_4 we can see V_{ref} determines the value of a_4 largely, which represents the strength of the coupling between the two subsystems. When V_{ref} increases, the coupling strength weakens and QS lasts shorter time. The qualitative dynamics with the variation of the coupling strength are shown in Figure 11. It can be found that the duration T of QS decreases quickly as V_{ref} increases. As is shown in Figure 11, when $V_{ref} = 5$ V, $T = 87.41$; when $V_{ref} = 10$ V, $T = 62.74$; and when $V_{ref} = 15$ V, $T = 48.14$.

3.4. Mechanism Analysis Based on Homotopy Method. According to the analysis above, the transient fixed points curves obtained possesses Hopf bifurcation points at which the full-system can be divided into a stable part and an unstable part, and qualitative dynamics is closely bound up with the properties of the transient fixed points. Therefore, the mechanism analysis of the bifurcation of the transient fixed points can give an intuitive explanation of the origin of complex oscillations of the full-system. A state-to-eigenvalue correspondence can be set up to reveal the physical mechanism of the qualitative dynamics by tracing the changing trend of the eigenvalues. The homotopy method [24–26] can be applied to link eigenvalues of the Jacobian matrix $J(X)$ of a dynamic model to the corresponding state variables through the following homotopy relation:

$$\mathbf{H}(r) = (1 - r)\mathbf{F}(X) + r\mathbf{J}(X) \quad (0 \leq r \leq 1), \quad (10)$$

where $\mathbf{F}(X) = \text{diag}[J_{11}, J_{22}, J_{33}, J_{44}, J_{55}, J_{66}]$ is the diagonal Jacobian and r is the homotopy parameter. When r varies in the interval $[0, 1]$ and the difference between each two adjacent values is sufficiently small, homotopy method takes the trajectory of eigenvalues of $\mathbf{H}(r)$ as a continuous path. Following the paths from $r = 0$ to $r = 1$, the correspondence between eigenvalues and state variables of the fast subsystem is established. Parameters are set as Table 3, and Figure 12 shows the trace of the sorted eigenvalues by making r as abscissa and the real part of eigenvalues of $\mathbf{H}(r)$ as vertical coordinate at $V_{ref} = 10$ V, $\bar{X}_5 = 0.9$. More traces are calculated and show the same correspondence, which is shown in Table 4.

From the analysis above, Hopf bifurcation occurs when λ_1 and λ_2 cross the imaginary axis. Thus λ_1 and λ_2 are the key factors which dominate the stability of the FESS. Considering the correspondence between the eigenvalues and the state variables, we can conclude that the system instability derives from the voltage instability; that is, the voltage instability is

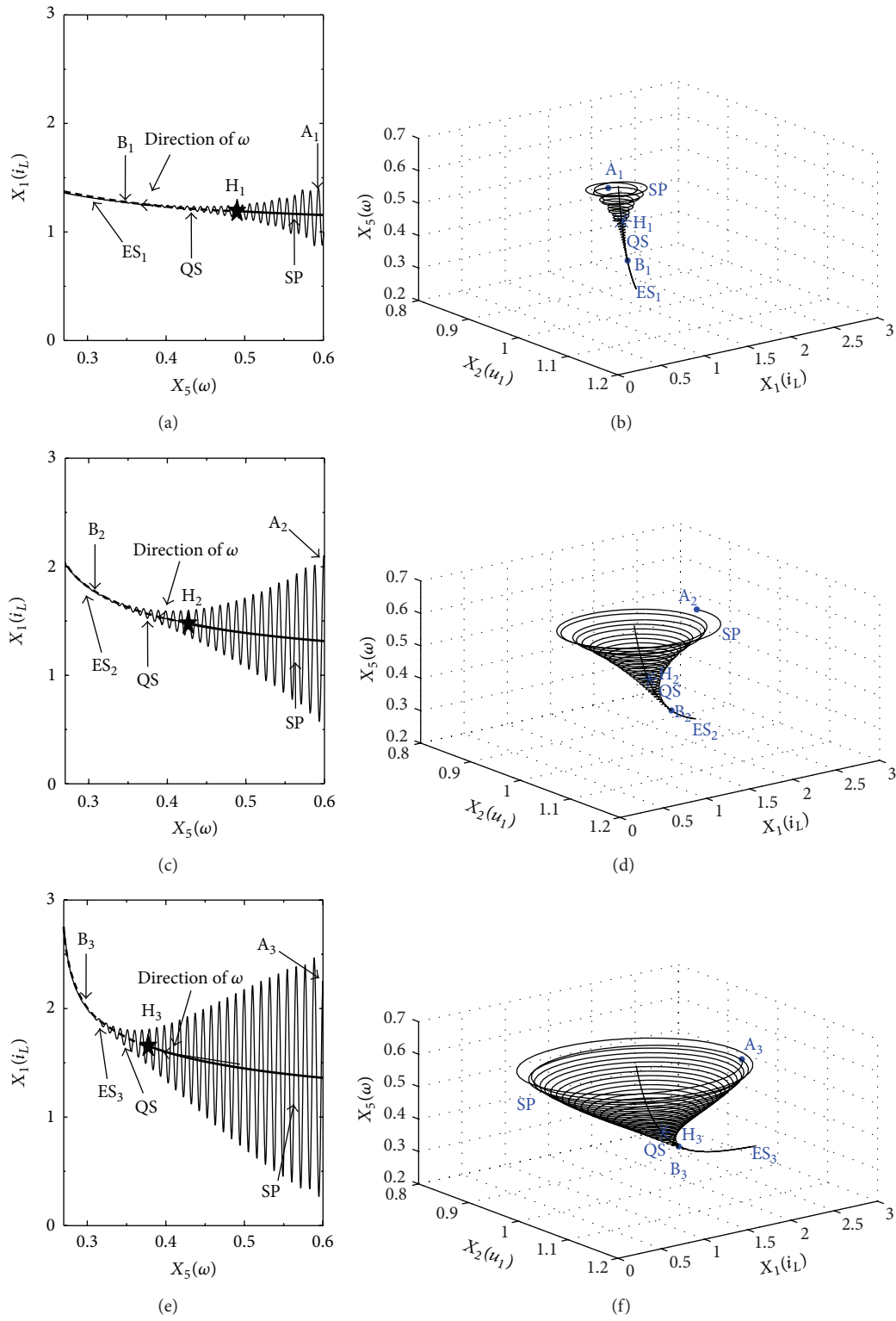


FIGURE 10: Stroboscopic phase trajectory of the full-system as well as the transient fixed points curves under different V_{ref} in two and three dimensions at (a)-(b) $V_{ref} = 5$ V, (c)-(d) $V_{ref} = 10$ V, and (e)-(f) $V_{ref} = 15$ V.

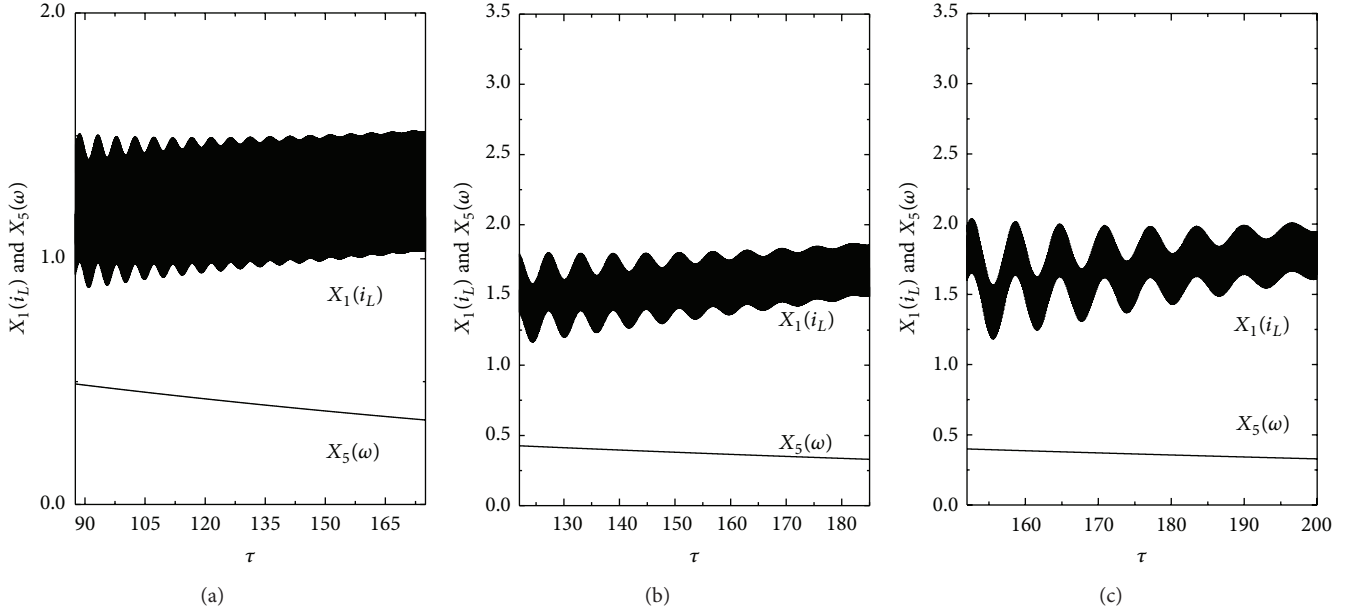


FIGURE 11: Time domain waveforms of QS at (a) $V_{\text{ref}} = 5$ V, (b) $V_{\text{ref}} = 10$ V, and (c) $V_{\text{ref}} = 15$ V.

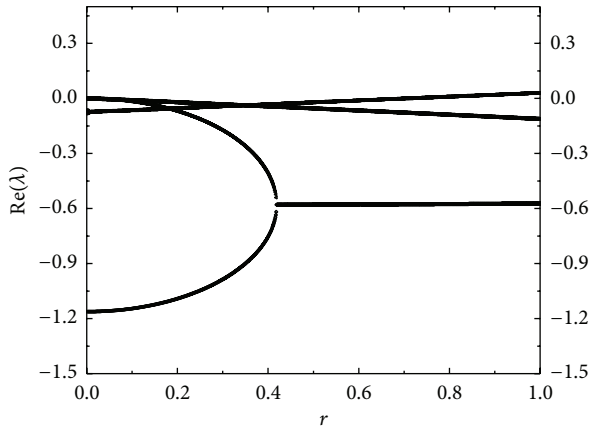


FIGURE 12: Real part of eigenvalues trace through homotopy method for FESS.

TABLE 4: The correspondence between eigenvalues and state variables.

State variables	eigenvalue
$X_2(u_1), X_3(u_2)$	λ_1, λ_2
$X_1(i_L), X_4(i_a)$	λ_3, λ_4
$X_6(x_{1c}), X_7(x_{2c})$	λ_5, λ_6

the root inducement of the qualitative dynamics. Therefore, dynamic voltage stability control scheme plays a key role in stabilizing the FESS, which will be the focus of our further work.

A detailed look into the influencing factors on the qualitative dynamics is taken further by presenting the boundaries

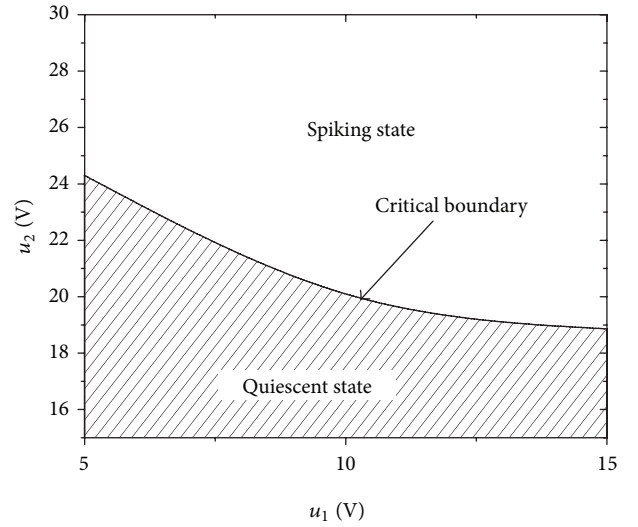


FIGURE 13: Critical boundary between SP and QS with $u_2 - u_1$.

of SP and QS in terms of u_2 and u_1 . It shows that the region of QS gets smaller with the increase of u_1 , which represents the load level (Figure 13).

4. Application

4.1. Feasibility Regions Analysis. This part will apply the two-timescale approach to derive the feasibility regions of FESS in the discharge mode and then provide instructions to parameters setting of FESS. From the analysis above we know that the feasibility regions of the fast subsystem dominate that of the full-system. Therefore, the FESS is stable when all

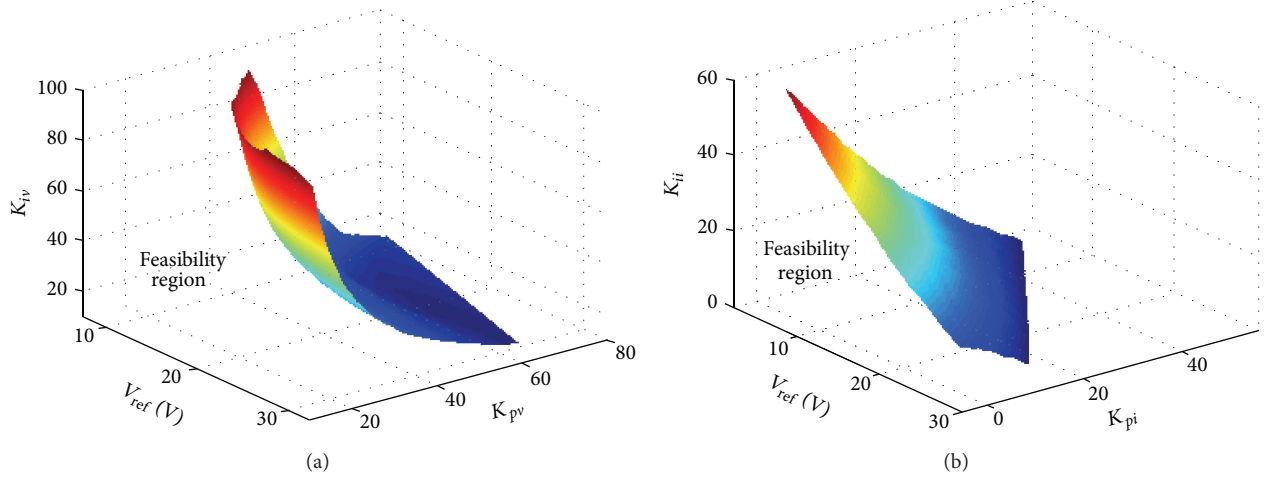


FIGURE 14: Feasibility regions of key parameters, (a) V_{ref} versus K_{pv} and K_{iv} at $K_{pi} = 40$, $K_{ii} = 36$, (b) V_{ref} versus K_{pi} and K_{ii} at $K_{pv} = 60$, $K_{iv} = 49$.

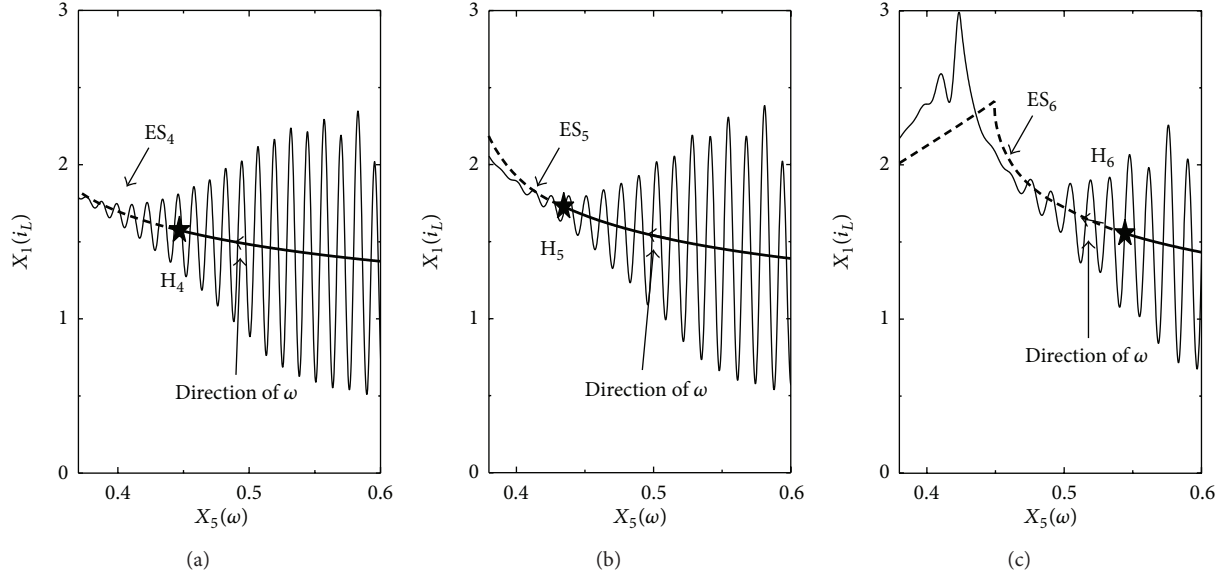


FIGURE 15: Stroboscopic phase trajectory of the full-system in $X_5(\omega) - X_1(i_L)$ as well as the transient fixed points curves at (a) $J' = 0.5 \cdot J$, (b) $J' = 0.25 \cdot J$, and (c) $J' = 0.1 \cdot J$. H_4 , H_5 , and H_6 -Hopf bifurcation point.

the eigenvalues of the fast subsystem are in the left half-side of complex plane with $X_5(\omega)$ decreasing from 1 to 0.

The feasibility regions of key parameters are shown in Figure 14. Figure 14(a) shows the feasibility boundary in the parameter space of V_{ref} versus the outer loop control parameters K_{pv} and K_{iv} and Figure 14(b) shows the feasibility boundary in the parameter space of V_{ref} versus the inner loop control parameters K_{pi} and K_{ii} , all of which clearly illustrate the effect of those sensitive parameters on the feasibility regions. The space in front of the critical surface corresponds to stable operation and the space behind it corresponds to unstable operation. The results can be used as instructions to the parameters setting of the access unit of FESS itself and constraints to improve the safety and stability of FESS and the power system.

4.2. Application Requirements. Obviously, the applicability and rationality of the proposed two-timescale approach with transient fixed points analysis mainly depend on the existence of state variables with two timescales, which is not to be considered as an exact criterion but as a guideline [27]. From model (7) we can see $a_7 = -K_m V_{ref} \sqrt{LC_1} / (J R \omega_{ref})$ and $a_8 = -B_v \sqrt{LC_1} / J$ represent the change rates of $X_5(\omega)$; thus, J dominates the difference between the fast and slow variables on timescales. For typical electromechanical coupling systems, the two-timescale characteristics are ubiquitous but in degree. As is shown in the foregoing analysis, the proposed approach does well in predicting the qualitative dynamics when the magnitude difference of fast and slow variables is about 100 times. Set J to 0.5, 0.25, and 0.1 times of its original value; other parameters are set as Table 3; then

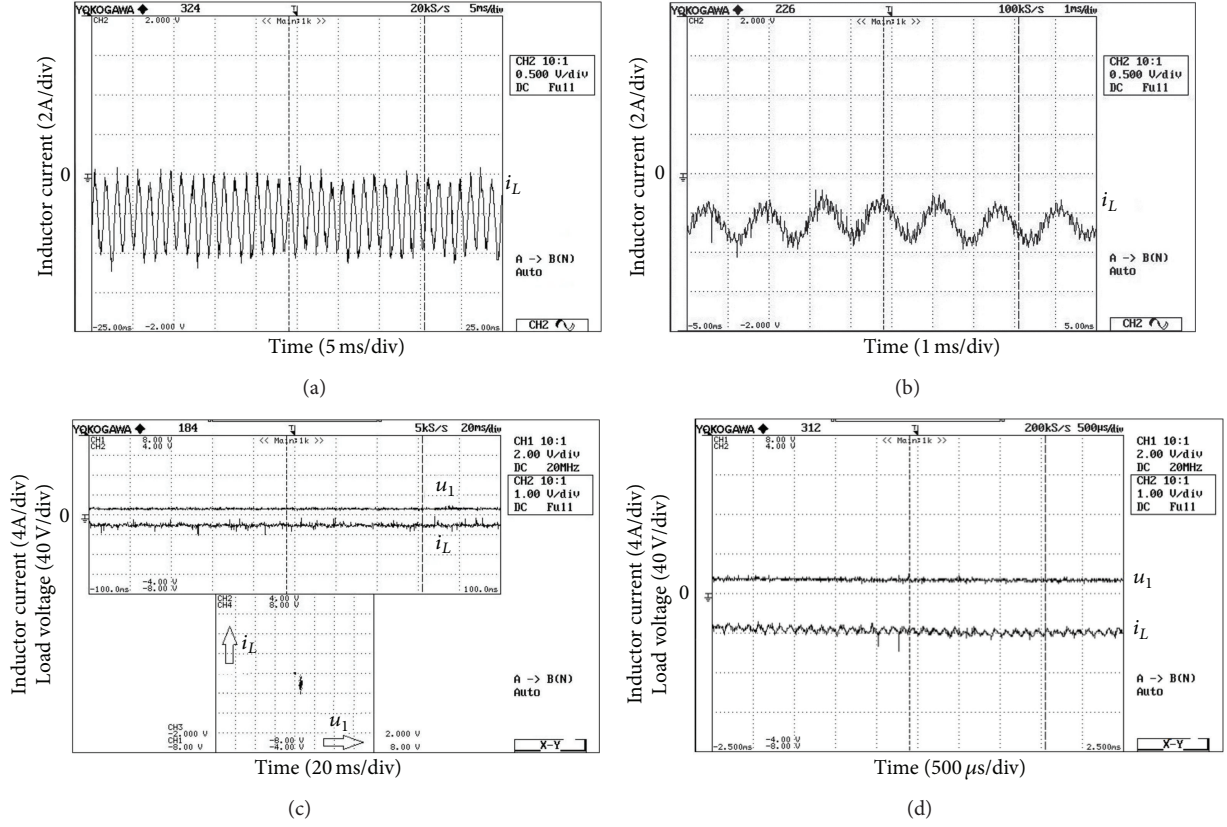


FIGURE 16: Discharge experiment for $V_{\text{ref}} = 15 \text{ V}$, (a) $X_5(\omega) = 0.60$, (b) $X_5(\omega) = 0.37$, (c) $X_5(\omega) = 0.25$, and (d) $X_5(\omega) = 0.20$.

the corresponding magnitude difference will be 50, 25, and 10 times. Figure 15 shows the stroboscopic phase trajectory of the full-system in the phase plane $X_5(\omega) - X_1(i_L)$ as well as the transient fixed points bifurcation diagram at $V_{\text{ref}} = 10 \text{ V}$. At $J' = 0.5 \cdot J$ in Figure 15(a), H_4 divides the phase trajectory of the full-system into two qualitatively different parts, which agrees very well with ES_4 . At $J' = 0.25 \cdot J$ in Figure 15(b), ES_5 basically corresponds to the dynamics of the full-system. At $J' = 0.1 \cdot J$ in Figure 15(c), ES_6 has deviated from the correct equilibrium position.

Considering that the two-timescale approach based on singular perturbation theory is a kind of model reduction method, Ghorbel and Spong [28] have given out the condition for the reduction of multitimescales system model; the equilibrium of the fast system must be close to that of the full-system. We can see that though the SP and QS caused by Hopf bifurcation are especially apparent in qualitative dynamics, they can still become weakening or even disappear as the difference of state variables on timescales diminishes. And meanwhile, the deviation between the transient fixed points curves and the stroboscopic phase trajectory of the full-system becomes larger, which reflects the inapplicability of the proposed approach. Therefore, the applicability and rationality of the proposed approach we concern here mainly refers to the bifurcation characteristics of the fast subsystem can actually reflect what extent of the full-system's dynamical evolution. From the numerical simulations in Figure 15

we can see the proposed approach is applicable when the magnitude difference of state variables is bigger than 25 times; more simulations have been done and gave out the same conclusion that when the magnitude difference is not big enough, the proposed approach is not applicable.

5. Experimental Verification

To verify the analysis in this paper, constant voltage discharge experiment is carried out; the parameter values are set as those in Table 3. The driving motor of the flywheel was solved by BLDCM, which indicates high reliability and the rotational speed being up to 8000 r/min. First charge up the FESS to 60% of its rated speed; then catch the time-variant dynamics under discharge mode at different V_{ref} . Set $V_{\text{ref}} = 15 \text{ V}$; the trajectory of i_L evolves with ω ; when $X_5(\omega) = 0.60$ (60% of rated speed) in Figure 16(a), i_L shows a large-scale oscillation with a frequency of 666.7 Hz and an amplitude of 4 A, implying the FESS is in SP; when $X_5(\omega) = 0.37$ in Figure 16(b), the amplitudes of quasiperiodic oscillation behaviors decrease gradually and approach a nearly stable limit cycle, as the property by Hopf bifurcation of the fast subsystem. The waveform of i_L is superposed with a sinusoidal oscillation with a frequency of 625 Hz and an amplitude of 2.4 A; then it settles down to QS; when $X_5(\omega) = 0.25$ and $X_5(\omega) = 0.20$ in Figures 16(c)-16(d), the phase trajectory of $i_L - u_L$ is a point and the FESS operates steady.

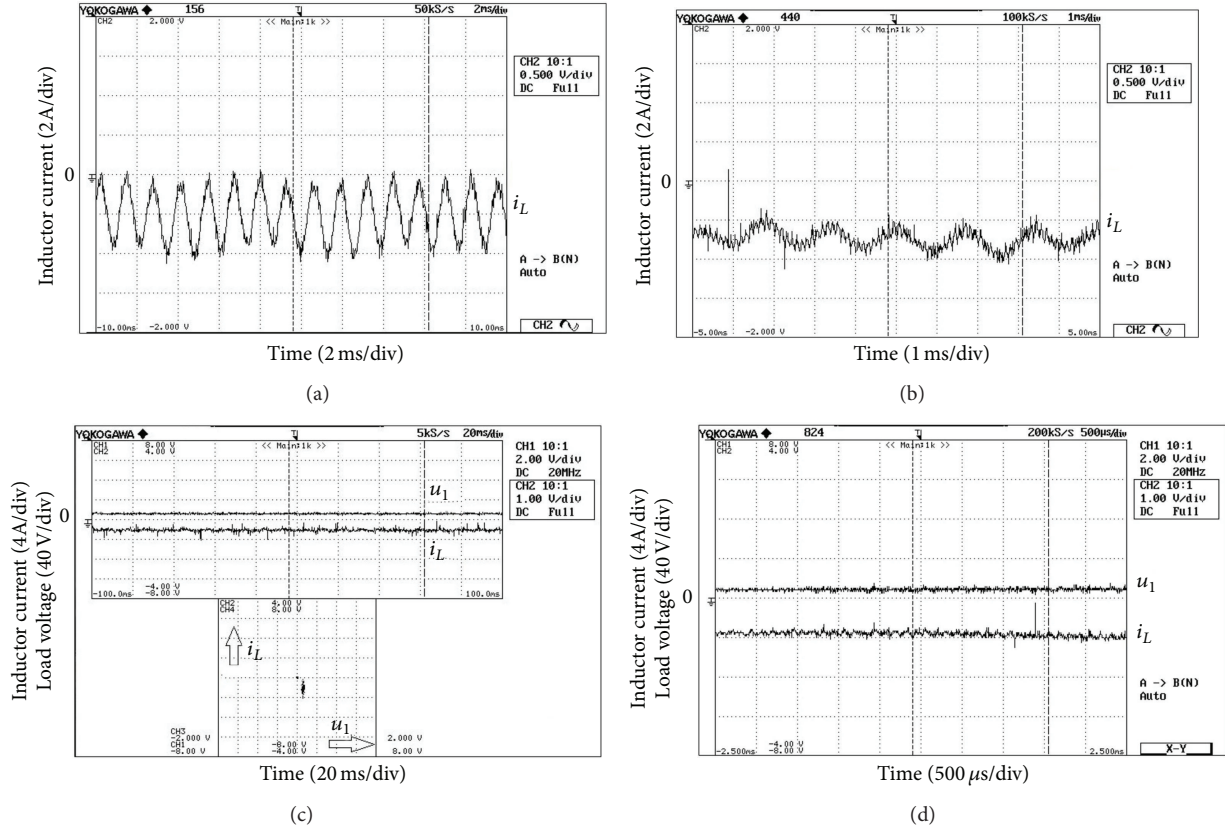


FIGURE 17: Discharge experiment for $V_{\text{ref}} = 10 \text{ V}$, (a) $X_5(\omega) = 0.60$, (b) $X_5(\omega) = 0.42$, (c) $X_5(\omega) = 0.25$, and (d) $X_5(\omega) = 0.20$.

The structures of qualitative dynamics change with V_{ref} . Figures 17-18 present phase portraits for $V_{\text{ref}} = 10 \text{ V}$ and $V_{\text{ref}} = 5 \text{ V}$, respectively. Set $V_{\text{ref}} = 10 \text{ V}$; when $X_5(\omega) = 0.60$ in Figure 17(a), i_L shows a large-scale oscillation with a frequency of 625 Hz and an amplitude of 4 A; when $X_5(\omega) = 0.42$ in Figure 17(b), the waveform of i_L mixes with a sinusoidal oscillation with a frequency of 588 Hz and an amplitude of 2 A; when $X_5(\omega) = 0.25$ and $X_5(\omega) = 0.20$ in Figures 17(c)-17(d), the phase trajectory of i_L - u_L is a point and the FESS operates steady. Set $V_{\text{ref}} = 5 \text{ V}$; when $X_5(\omega) = 0.60$ in Figure 18(a), i_L shows a large-scale oscillation with a frequency of 600 Hz and an amplitude of 3.8 A; when $X_5(\omega) = 0.49$ in Figure 18(b), the waveform of i_L mixes with a sinusoidal oscillation with a frequency of 90 Hz and an amplitude of 0.67 A; when $X_5(\omega) = 0.25$ and $X_5(\omega) = 0.20$ in Figures 18(c)-18(d), the phase trajectory of i_L - u_L is a point and the FESS operates steady.

6. Conclusion

This paper investigates the qualitative dynamics of the voltage-current dual-loop controlled FESS, which is mainly shown as the fast oscillations of the inductor current and the motor voltage weakens along with the slowdown of the flywheel rotor. By the proposed two-timescale approach based on singular perturbation theory, the state variables are separated into fast and slow variables. First, it is shown

that the stability of FESS is closely bound up with that of the transient fixed points. The FESS shifts from SP to QS when the slow variable crosses the bifurcation point on the transient fixed points curve. Larger eigenvalues' real parts determine more intense oscillations in SP, and larger coupling coefficient leads to longer duration of QS. Further analysis shows that the evolution of the full-system's dynamics is dominated by the difference between the slow and fast variables on timescales, whereas the qualitative dynamics are mainly caused by the voltage instability. Moreover, the feasibility regions of the main system parameters are derived, in which stability operation and power transmission quality of FESS can be guaranteed. Finally, an applicability investigation shows that when the difference of state variables on timescales is not big enough, the proposed approach is not applicable. This paper provides insights into the effect of two-timescale characteristics on the safety and stability of energy transmission of FESS. The results can be used as instructions to the parameters setting of the FESS itself and constraints to improve the safety and stability of FESS and the smart grids.

Conflict of Interests

The authors declare that there is no conflict of interests regarding the publication of this paper.

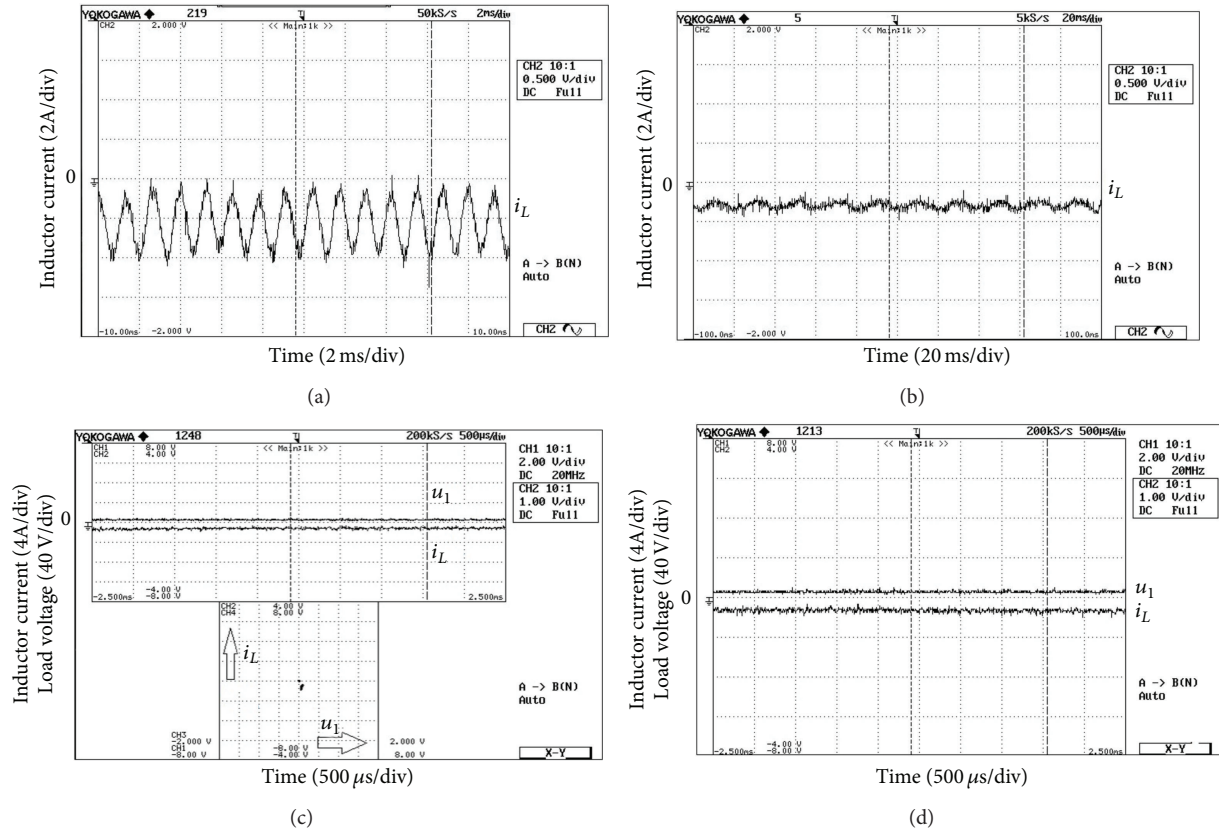


FIGURE 18: Discharge experiment for $V_{ref} = 5$ V, (a) $X_5(\omega) = 0.60$, (b) $X_5(\omega) = 0.49$, (c) $X_5(\omega) = 0.25$, and (d) $X_5(\omega) = 0.20$.

Acknowledgments

This work was supported in part by the National Basic Research Program of China (Grant no. 2009CB2197), the National Natural Science Foundation of China (Grant no. 51177108), and the Specialized Research Fund for the Doctoral Program of Higher Education of China (Grant no. 20110032110066).

References

- [1] B. Szabados and U. Schaible, "Peak power Bi-directional transfer from high speed flywheel to electrical regulated bus voltage system: a practical proposal for vehicular technology," *IEEE Transactions on Energy Conversion*, vol. 13, no. 1, pp. 34–41, 1998.
- [2] R. Cárdenas, R. Peña, G. Asher, and J. Clare, "Power smoothing in wind generation systems using a sensorless vector controlled induction machine driving a flywheel," *IEEE Transactions on Energy Conversion*, vol. 19, no. 1, pp. 206–216, 2004.
- [3] G. Duan and D. Howe, "Robust magnetic bearing control via eigenstructure assignment dynamical compensation," *IEEE Transactions on Control Systems Technology*, vol. 11, no. 2, pp. 204–215, 2003.
- [4] Y. Ren, D. Su, and J. C. Fang, "Whirling modes stability criterion for a magnetically suspended flywheel rotor with significant gyroscopic effects and bending modes," *IEEE Transactions on Power Electronics*, vol. 28, no. 12, pp. 5890–5901, 2013.
- [5] J. T. Tzeng, "Mechanics of composite rotating machines for pulsed power applications," *IEEE Transactions on Magnetics*, vol. 37, no. 1, pp. 328–331, 2001.
- [6] J. Choi, S. Jang, S. Sung et al., "Operating range evaluation of double-side permanent magnet synchronous motor/generator for flywheel energy storage system," *IEEE Transactions on Magnetics*, vol. 49, no. 7, pp. 4076–4079, 2013.
- [7] M. Komori and Y. Uchimura, "Improving the dynamics of two types of flywheel energy storage systems with SMBs," *IEEE Transactions on Applied Superconductivity*, vol. 15, no. 2, pp. 2261–2264, 2005.
- [8] H. Mitsuda, A. Inoue, B. Nakaya, and M. Komori, "Improvement of energy storage flywheel system with SMB and PMB and its performances," *IEEE Transactions on Applied Superconductivity*, vol. 19, no. 3, pp. 2091–2094, 2009.
- [9] J.-D. Park, C. Kalev, and H. F. Hofmann, "Analysis and reduction of time harmonic rotor loss in solid-rotor synchronous reluctance drive," *IEEE Transactions on Power Electronics*, vol. 23, no. 2, pp. 985–992, 2008.
- [10] W.-Y. Zhang, Y.-L. Li, X.-Y. Chang, and N. Wang, "Dynamical investigation and parameter stability region analysis of a flywheel energy storage system in charging mode," *Chinese Physics B*, vol. 22, no. 9, Article ID 098401, pp. 1–14, 2013.
- [11] H. Hofmann and S. R. Sanders, "Speed-sensorless vector torque control of induction machines using a two-time-scale approach," *IEEE Transactions on Industry Applications*, vol. 34, no. 1, pp. 169–177, 1998.

- [12] J. Van Pelt, P. S. Wolters, M. A. Corner, W. L. C. Rutten, and G. J. A. Ramakers, "Long-term characterization of firing dynamics of spontaneous bursts in cultured neural networks," *IEEE Transactions on Biomedical Engineering*, vol. 51, no. 11, pp. 2051–2062, 2004.
- [13] T. Yu, T. J. Sejnowski, and G. Cauwenberghs, "Biophysical neural spiking, bursting, and excitability dynamics in reconfigurable analog VLSI," *IEEE Transactions on Biomedical Circuits and Systems*, vol. 5, no. 5, pp. 420–429, 2011.
- [14] M. Diener, "The canard unchained or how fast/slow dynamical systems bifurcate," *The Mathematical Intelligencer*, vol. 6, no. 3, pp. 38–49, 1984.
- [15] E. F. Mishchenko and N. K. Rozov, *Differential Equations with Small Parameters and Relaxation Oscillations*, vol. 13 of *Mathematical Concepts and Methods in Science and Engineering*, Plenum Press, New York, NY, USA, 1980.
- [16] C. K. R. Jones, "Geometric singular perturbation theory," in *Dynamical Systems*, vol. 1609 of *Lecture Notes in Mathematics*, pp. 44–118, Springer, New York, NY, USA, 1995.
- [17] J. Rinzel, "Bursting oscillations in an excitable membrane model," in *Ordinary and Partial Differential Equations: Proceedings of the 8th Conference*, B. D. Sleeman and R. J. Jarvis, Eds., vol. 1151 of *Lecture Notes in Mathematics*, pp. 304–316, Springer, Berlin, Germany, 1985.
- [18] S. D. Pekarek, M. T. Lemanski, and E. A. Walters, "On the use of singular perturbations to neglect the dynamic saliency of synchronous machines," *IEEE Transactions on Energy Conversion*, vol. 17, no. 3, pp. 385–391, 2002.
- [19] N. Milivojevic, M. Krishnamurthy, A. Emadi, and I. Stamenkovic, "Theory and implementation of a simple digital control strategy for brushless DC generators," *IEEE Transactions on Power Electronics*, vol. 26, no. 11, pp. 3345–3356, 2011.
- [20] C. K. Tse, Y. M. Lai, and H. H. C. Lu, "Hopf bifurcation and chaos in a free-running current-controlled Cuk switching regulator," *IEEE Transactions on Circuits and Systems I: Fundamental Theory and Applications*, vol. 47, no. 4, pp. 448–457, 2000.
- [21] H. H. C. Lu and C. K. Tse, "Study of low-frequency bifurcation phenomena of a parallel-connected boost converter system via simple averaged models," *IEEE Transactions on Circuits and Systems I: Fundamental Theory and Applications*, vol. 50, no. 5, pp. 679–686, 2003.
- [22] E. M. Izhikevich, *Dynamical Systems in Neuroscience: The Geometry of Excitability and Bursting*, Computational Neuroscience, MIT Press, Cambridge, Mass, USA, 2007.
- [23] C. S. Tang, Y. Sun, Y. G. Su, S. K. Nguang, and A. P. Hu, "Determining multiple steady-state ZCS operating points of a switch-mode contactless power transfer system," *IEEE Transactions on Power Electronics*, vol. 24, no. 2, pp. 416–425, 2009.
- [24] R. C. Melville, L. Trajković, S. Fang, and L. T. Watson, "Artificial parameter homotopy methods for the DC operating point problem," *IEEE Transactions on Computer-Aided Design of Integrated Circuits and Systems*, vol. 12, no. 6, pp. 861–877, 1993.
- [25] G. A. Robertson and I. T. Cameron, "Analysis of dynamic process models for structural insight and model reduction Part 1: structural identification measures," *Computers and Chemical Engineering*, vol. 21, no. 5, pp. 455–473, 1997.
- [26] J. E. Bergner, "Three models for the homotopy theory of homotopy theories," *Topology*, vol. 46, no. 4, pp. 397–436, 2007.
- [27] T. J. Kaper, "An introduction to geometric methods and dynamical systems theory for singular perturbation problems," *Proceedings of Symposia in Applied Mathematics*, vol. 56, pp. 85–131, 1999.
- [28] F. Ghorbel and M. W. Spong, "Integral manifolds of singularly perturbed systems with application to rigid-link flexible-joint multibody systems," *International Journal of Non-Linear Mechanics*, vol. 35, no. 1, pp. 133–155, 2000.

